Comparison of magnetic couplers for IPT-based EV charging using multi-objective optimization

Bandyopadhyay, Soumya; Prasanth, Venugopal; Dong, Jianning; Bauer, Pavol

DOI
10.1109/TVT.2019.2909566

Publication date
2019

Document Version
Final published version

Published in
IEEE Transactions on Vehicular Technology

Comparison of Magnetic Couplers for IPT-Based EV Charging Using Multi-Objective Optimization

Soumya Bandyopadhyay, *Student Member, IEEE*, Prasanth Venugopal, *Member, IEEE*, Jianning Dong, *Member, IEEE*, and Pavol Bauer, *Senior Member, IEEE*

***Abstract*—Inductive power transfer (IPT) is becoming increasingly popular in stationary electric vehicle (EV) charging systems. In this paper, the influence of the different IPT coupler geometries on the performance factors such as efficiency, power density, misalignment tolerance, and stray field is studied. Four different coupler topologies, namely the circular, rectangular, double-D (DD-DD), and the double-D transmitter with double-D-quadrature receiver (DD-DDQ) are considered in this study. The electromagnetic behavior of the couplers is modeled using three-dimensional finite-element method, which is validated by experiments on a laboratory prototype. A multi-objective optimization (MOO) framework is developed to analyze the Pareto tradeoffs between conflicting performance metrics for the couplers. Optimization results depict that the circular topology performs best among the selected topologies regarding higher coupling coefficient, and efficiency for similar active mass and coupler area. Circular and rectangular couplers perform better than the polarized couplers like DD-DD and DD-DDQ regarding stray field exposure in both vertical and lateral direction of the coupler position in the EV. However, polarized couplers show more tolerance toward misalignment compared to circular and rectangular couplers. Thus, this study provides information regarding the specific strengths and weaknesses of different coupler topologies, which can be used during the initial design phase.**

***Index Terms*—Coupling, electric vehicles, finite element analysis, inductive power transmission, lateral misalignment, longitudinal misalignment, Pareto optimization.**

I. Introduction

INDUCTIVE power transfer (IPT) is a popular solution for a wide range of battery charging applications, such as low power bio-medical implants, industrial automation, consumer electronics and electric vehicles (EVs) [1], [2]. IPT technology for EV charging is more user-friendly and safe than conventional wired charging due to the absence of electrical or mechanical contacts. Additionally, it opens up the possibility of dynamically charging the EV battery while they are running [3], [4]. Due to these advantages as mentioned above, IPT technology is a crucial enabling factor for a further increase in the popularity of EVs.

A large number of coupler topologies for IPT based EV charging is reported in literature [5]–[8]. Based on coil winding strategy, there can be two types of lumped IPT charge pads: a) Solenoid or double sided flux couplers [7], [9] and b) planar or single-sided flux couplers [5]. Planar couplers can be further classified into two families based on fundamental flux path: a) non-polarized couplers like circular and rectangular geometries [10]–[12] and b) multi-coil polarized couplers like double D (DD) [6], [13], bi-polar pad (BPP) [14], and double D-Quadrature (DDQ) [5], [8], [15].

Comparisons between different concepts are found in several publications [16]–[19]. Several coil topologies are compared using numerical methods and statistical methods in [16], [17]. However, in those studies different loss mechanisms in the charge pads are not considered. Also, the advantages of the various coil topologies of primary performance factors like power transfer efficiency, power densities, misalignment tolerance, and stray field exposure are not clear. To ensure a fair quantitative comparison, the IPT couplers considered should be optimized under given constraints. A multi-objective optimization approach is introduced in [20], [21], where design tradeoffs between efficiency (η), area power density (α) and gravimetric power density (γ) in the form of Pareto fronts are presented. However, the study was limited to only two coupler geometries and didn't consider the trade-offs between misalignment tolerance and power densities of the couplers.

This paper extends the above studies to include all major topologies and performance parameters. The objective of this paper is to compare the following coupler geometries:

1) Circular (Transmitter + Receiver)
2) Rectangular (Transmitter + Receiver)
3) DD (Transmitter + Receiver)
4) DD (Transmitter) - DDQ (Receiver)

To ensure a fair comparison, the chosen coupler geometries are optimized with the goal of maximizing efficiency, vehicle pad area power density, gravimetric power density, and misalignment tolerance.

To that end, the main contributions of the paper are:

1) Developing computationally efficient numerical modeling methodology of IPT couplers suitable for optimization.
2) Validating the developed numerical modeling methodology with experimental tests.
3) Developing a generalized multi-objective optimization (MOO) framework for design of IPT coupler.
4) The developed and validated modeling methodology is combined with the MOO framework to assess the performance of the four popular coupler topologies (see

Manuscript received August 2, 2018; revised December 13, 2018; accepted March 28, 2019. Date of publication April 9, 2019; date of current version June 18, 2019. This work was supported by the NWO, Netherlands. The review of this paper was coordinated by Prof. A. Rathore. *(Corresponding author: Soumya Bandyopadhyay.)*

S. Bandyopadhyay, J. Dong, and P. Bauer are with the DCE&S/EEMCS, Technische Universiteit Delft, Delft 2624 CP, The Netherlands (e-mail: s.bandyopadhyay-1@tudelft.nl; j.dong-4@tudelft.nl; p.bauer@tudelft.nl).

P. Venugopal is with the TDK Europe Gmbh, Munich 81671, Germany (e-mail: vprasanth@ieee.org).

Digital Object Identifier 10.1109/TVT.2019.2909566

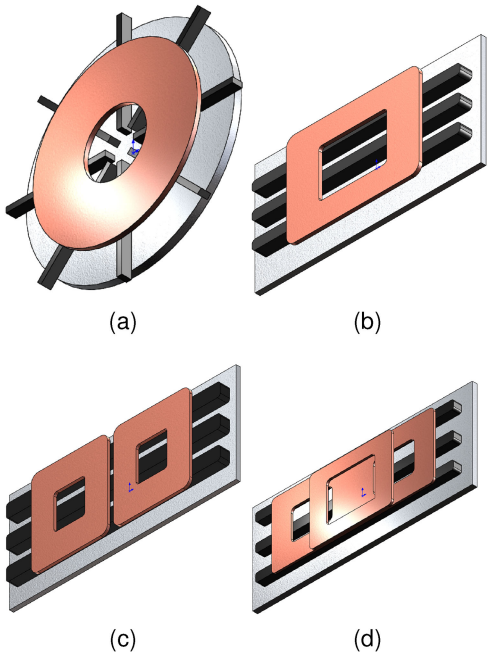

Fig. 1. Selection of couplers for optimization and comparison: (a) Circular, (b) Rectangular, (c) DD, and (d) DDQ.

Figure 1) and presents the merits and demerits of individual concepts.

5) Highlighting trade-offs and trends among the performance parameters (efficiency, power density, misalignment tolerance and stray field) for all the coupler geometries.

The paper is structured in five parts. In Section II, the numerical modeling methodology is discussed briefly. Section III validates the numerical modeling methodology with experiments. Section IV develops the multi-objective optimization (MOO) framework, and optimizes the different couplers utilizing the validated modeling methodology and presents a detailed comparative analysis of the coupler topologies based on optimization results. Finally, general conclusions are summarized based on the results.

II. Modeling the Magnetic Coupler Concepts

The couplers selected for comparative analysis are be modeled and analyzed in this section. Finite element (FE) analysis is used to model the coupler electromagnetics. The resulting data is post-processed to extract the losses in the coupler along with other performance metrics.

A. 3D Model Simplification and Assumptions

COMSOL, a commercially available FE software is used to model the couplers. The considered couplers consist of distributed ferrite strips as shown in Figure 1. Hence, 3D finite element (FE) models are necessary to compute their electromagnetic behavior. However, this leads to the longer computation time for individual models. To make the 3D models suitable for optimization purposes, geometrical symmetries of the couplers are exploited to reduce the model. A combination of symmetry boundary conditions like the parallel flux, normal flux, and periodic boundary conditions [22] are used to reduce the computational loads of the 3D models by several orders.

Automated physics based meshing is used in the 3D models which leads to optimal mesh sizes for different materials based on their skin depths. The litz wire winding is a 3D lumped model for a bundle of tiny wires tightly wound together with uniform current density, separated by an electrical insulator. This prevents the intensive computation load associated with the calculation of the eddy currents in the winding. This approximation is valid since: (1) since litz wire is composed of sinusoidally woven insulated strands of copper, the equal current distribution is a good assumption given they have symmetric impedances, (2) the litz wire strand diameter is chosen accordingly to render the high-frequency effects to a minimum, (3) the current distribution in the windings have small effect on the computation of the inductance of the coupler geometries, and (4) the losses in the windings are computed using analytical equations combined with field values derived separately from a 2D FE model. To further reduce the computation time, linear ferrites are considered with fixed relative permeability ($\mu_{\mathrm{r}} = 2500$). This approximation is valid since a hard constraint is placed on the maximum flux density ($B_{\max}$) of the cores during optimization. $B_{\max}$ is strategically chosen well below the saturation flux density of the core material used.

B. Power Loss Calculation

Coupler losses are computed by analytical post-processing in MATLAB by extracting magnetic field data from the FE models. The IPT system losses consist of: (a) coupler (litz wire, ferrite, aluminium), (b) compensation capacitors, and (c) power electronics. They are briefly discussed in this section.

The litz copper loss (P_{cu}) is comprised of dc ohmic losses (P_{dc}) and ac losses (P_{ac}) due to skin effect and proximity effect (internal and external). They are computed using the following equations [23]:

$$P_{\mathrm{skin}} + P_{\mathrm{dc}} = n_{\mathrm{str}} r_{\mathrm{dc}} F_{\mathrm{R}}(f_0) \left(\frac{\hat{I}}{n_{\mathrm{str}}} \right)^2 L_{\mathrm{coil}} \tag{1}$$

$$\begin{aligned} P_{\mathrm{prox,tot}} &= P_{\mathrm{prox,int}} + P_{\mathrm{prox,ext}} \\ &= n_{\mathrm{str}} r_{\mathrm{dc}} G_{\mathrm{R}}(f_0) \frac{\hat{I}^2}{2\pi^2 d_a^2} L_{\mathrm{coil}} \\ &\quad + \sum_{i=i}^{N} n_{\mathrm{str}} r_{\mathrm{dc}} G_{\mathrm{R}}(f_0) \int_{l_i} \hat{H_{\mathrm{ext}}}(l)^2 \mathrm{dl} \end{aligned} \tag{2}$$

where n_{str} denotes the number of strands in the litz wire, r_{dc} is the dc resistance per unit length of unit strand of the litz wire, $\hat{H_{\mathrm{ext}}}$ is the external magnetic field penetrating the individual coil turns, $F_{\mathrm{R}}(f_0)$ and $G_{\mathrm{R}}(f_0)$ are frequency dependent factors. For accurate loss estimation, $\hat{H_{\mathrm{ext}}}$ is extracted from a 2D FE model data separately as shown in Figure 2 for each turn and summed. The ferrite core losses (P_{fe}) are determined using the Steinmetz equation and integrating it over the core volumes [24]:

$$P_{\mathrm{fe}} = \iiint_V \kappa f_0^{\alpha} \hat{B}^{\beta} dV \tag{3}$$

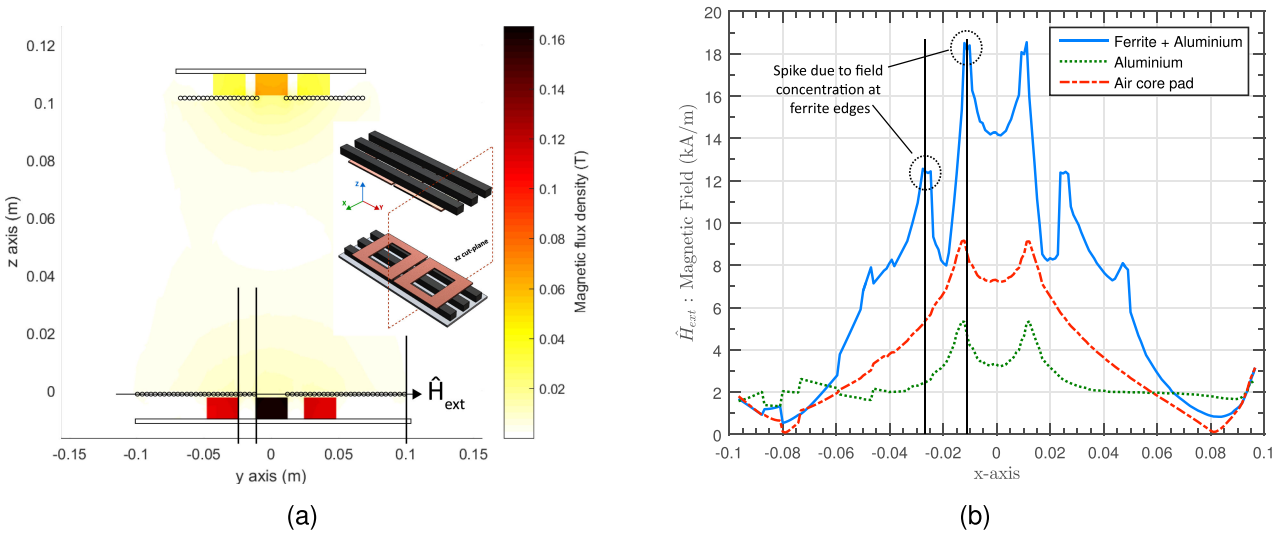

Fig. 2. Example of proximity loss computation in a DD coupler with 30 turns and 10 A peak current: (a) Surface magnetic flux density plot of a DD coupler in the xz plane for extraction of external magnetic field intensity ($\vec{H}_{\text{ext}}$) penetrating the turns in the coupler, (b) plot of magnetic field intensity ($\vec{H}_{\text{ext}}$) penetrating the transmitter coil turns. Presence of ferrite increases the H-field penetrating the coil turns while compared to an air core coil, especially for turns located at the edge of the ferrites. In the absence of ferrites, eddy currents induced in the aluminum shield reduces the H-field penetration since they oppose the magnetic field produced by the coil turns in accordance with Lenz's law.

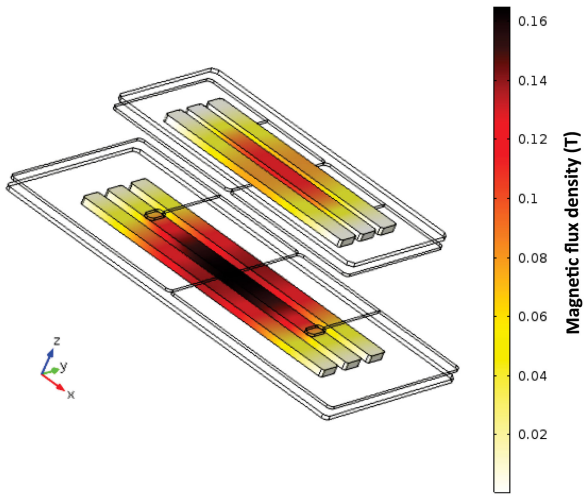

Fig. 3. Example of peak AC magnetic flux density distribution (T) in the ferrite cores of a DD coupler. The design of DD couplers is limited by the central region of the ferrites which carries the maximum flux.

where the Steinmetz parameters of the core material 3C-90 are $\kappa = 3.2\text{E-}3$, $\alpha = 1.46$ and $\beta = 2.75$. The peak AC flux density ($\hat{B}$) is extracted from the 3D FE models as highlighted in Figure 3. Loss due to eddy currents induced in the aluminium (P_{al}) is computed using the surface current density equation [25]:

$$P_{\text{al}} = \iint_A \frac{1}{2}(J_S.E^*)dA \tag{4}$$

where J_S is the induced surface current density on the aluminium sheets and E is the electric field at the surface boundary.

Polypropylene film capacitors from KEMET are considered for resonant compensation due to their relatively low dielectric losses. The capacitor dielectric loss is calculated according to the following equation [26]:

$$P_{\text{cap}} = \frac{\tan\delta}{\omega C} I_{\text{rms}}^2 \tag{5}$$

The dielectric loss factor $\tan\delta$ is chosen to be 0.1% at 100 kHz [27]. The power electronic losses include the losses in the inverter and the rectifier ($P_{\text{inv}}, P_{\text{rec}}$). SiC Schottky diodes (C4D40120D) and MOSFET (C2M0025120D) by Cree are considered for the device loss models. The switching and conduction losses are computed using the data provided in the manufacturer's datasheet and equations presented in [28].

Once all the losses in the couplers are computed resulting in total loss P_{tot}, the ac resistance (r_{ac}) of the individual couplers is given by the following equation:

$$r_{\text{ac}} = \frac{P_{\text{tot}}}{I^2} = \frac{P_{\text{al}} + P_{\text{fe}} + P_{\text{cu}}}{I^2} \tag{6}$$

where I is the driving current through a coupler. The total system transmission efficiency η_{T} is then determined by the following equation:

$$\eta_T = \eta_{\text{inv}}\eta_{\text{mag}}\eta_{\text{rec}} = \frac{P_{\text{out}}}{P_{\text{out}} + P_{\text{tot}} + P_{\text{inv}} + P_{\text{rec}}} \tag{7}$$

where P_{out} is the power output computed at the terminals of the rectifier, η_{inv} , η_{rec} , η_{mag} are the efficiencies of the inverter, rectifier, and couplers respectively (see Figure 4).

To improve efficiency performance during both aligned and mis-aligned conditions, the optimal load impedance matching algorithm with dual side control [20] is used which is briefly explained in the upcoming section.

C. Optimal Load Matching With Dual-Side Control

A dual sided control strategy [29] with optimal load matching algorithm is considered in this paper. Figure 4 depicts the overall IPT system with different conversion stages. The power

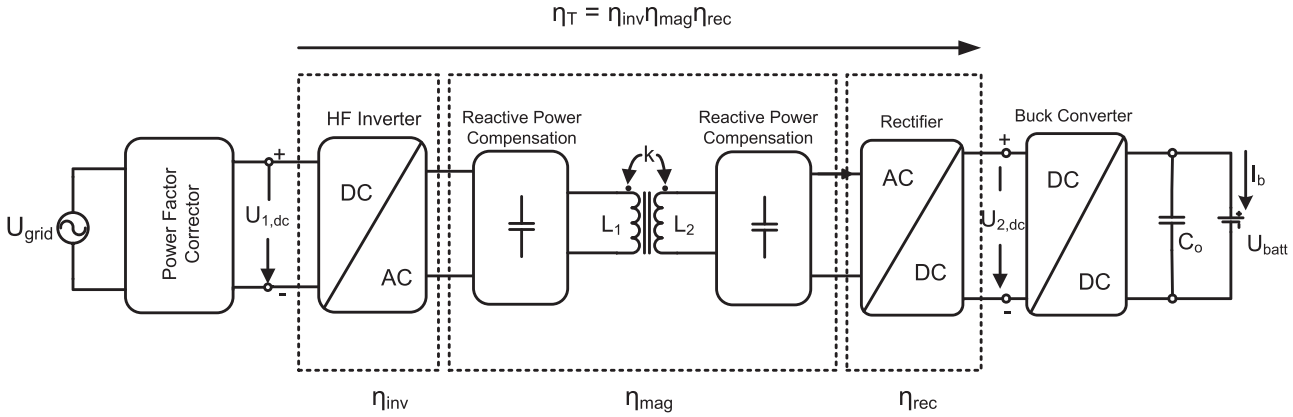

Fig. 4. The overall IPT system for EV charging from the grid to the battery is presented. In this paper, the efficiency of power transfer from the transmission side dc link ($U_{1,\mathrm{dc}}$) to the receiver side dc link ($U_{2,\mathrm{dc}}$). There are three power conversion stages in between: (a) the dc-ac stage of the high frequency inverter with efficiency η_{inv}, (b) the ac-ac stage of the magnetic couplers with efficiency η_{mag}, and (c) the ac-dc stage of the rectifier with efficiency η_{rec}. This leads to a total system power trnasmission efficiency of $\eta_{\mathrm{T}} = \eta_{\mathrm{inv}}\eta_{\mathrm{mag}}\eta_{\mathrm{rec}}$.

is controlled by varying the transmitter side dc voltage $\mathrm{U}_{1,\mathrm{dc}}$ and the receiver side dc voltage $\mathrm{U}_{2,\mathrm{dc}}$ based on the following:

$$P_{\mathrm{out}} = \frac{8}{\pi^2}\frac{U_{1,\mathrm{dc}}U_{2,\mathrm{dc}}}{\omega M} \tag{8}$$

where P_{out} is the reference power requested by the battery, ω is the angular frequency of the system, M is the mutual inductance between the couplers. The dc link voltage ($\mathrm{U}_{2,\mathrm{dc}}$) in the pickup circuit is controlled by a dc-dc converter before the battery. Optimal load impedance matching algorithm [20] is used in conjunction with dual-side control which results in maximum power transfer efficiency for a certain operating condition. However, the load impedance matching algorithm proposed in [20] is only applicable to systems with similar transmitter and receiver coupler designs. In this paper, the study is extended to compute the load matching factor with asymmetric transmitter and receiver designs which leads to the following condition for load matching:

$$R_{\mathrm{L,eq}} \approx \omega M\sqrt{\frac{r_{\mathrm{acR}}}{r_{\mathrm{acT}}}} \tag{9}$$

where r_{acT} and r_{acR} are the ac resistances of the transmitter and receiver couplers and $R_{\mathrm{L,eq}}$ is the effective equivalent load resistance of the pick up circuitry. A detailed derivation of (9) is provided in the Appendix. Accordingly, the reference value of the receiver dc link voltage $U^*_{2,\mathrm{dc}}$ (see Figure 4) during load impedance matching is determined using the following equation:

$$U^{*2}_{2,\mathrm{dc}} \approx \frac{\pi^2}{8}\eta_{\mathrm{rec}}\omega M P_{\mathrm{out}}\sqrt{\frac{r_{\mathrm{acR}}}{r_{\mathrm{acT}}}} \tag{10}$$

Therefore, $U^*_{2,\mathrm{dc}}$ is used as a set point to ensure maximum power transfer efficiency. To ensure power regulation, the set point value of the transmitter side dc link voltage $U^*_{1,\mathrm{dc}}$ is calculated based on the set point $U^*_{2,\mathrm{dc}}$.

During misalignment, the value of M changes which will lead to the change of set point value of $U^*_{2,\mathrm{dc}}$. Active impedance matching can still be executed on real time with a new estimate of coupling (k') and the new set point for the secondary dc link voltage will then be:

$$U'^*_{2,\mathrm{dc}} = U^*_{2,\mathrm{dc}}\sqrt{\frac{k'}{k}} \tag{11}$$

During operation, the coupling co-efficient or the mutual inductance can be estimated online by measuring the voltages and currents of the transmitter and receiver pads [30].

This concludes the numerical modeling strategy of the coupler concepts along with the system control strategy. Before utilizing the models to optimize and compare different coupler geometries, they need to be validated to establish confidence of trends derived from the optimization results. In the upcoming section, the modeling strategy is validated with experimental results.

III. Experimental Validation of Modeling Approach

The goal of this paper is to compare different coupler geometries by multi-objective optimization which is computationally intensive. Hence, a computationally efficient and reasonably accurate modeling approach is necessary. Section II introduces a computational-friendly axi-symmetric 3D FE based modeling strategy. To establish confidence in the modeling approach, time should be spent to examine the integrity of the results obtained before using the modeling strategy for optimization. Thus, this section will validate the accuracy of the developed modeling approach by experiments on a laboratory prototype. Since the same modeling strategy is utilized for the different coupler geometries, validating the modeling approach is sufficient. The accuracy of the modeling approach will be validated on three essential aspects: (a) magnetic and electrical parameters of the couplers, (b) loss prediction, and (c) stray field estimation. To that end, the experimental setup built for this purpose is discussed in the following section followed by comparing model generated results and experimentally obtained data.

In this paper, an IPT system with DD coils will be utilized to validate the modeling strategy. This system was initially designed for a power transfer rating of 2.5 kW across an air gap of 10.2 cm. The experimental IPT schematic and the laboratory

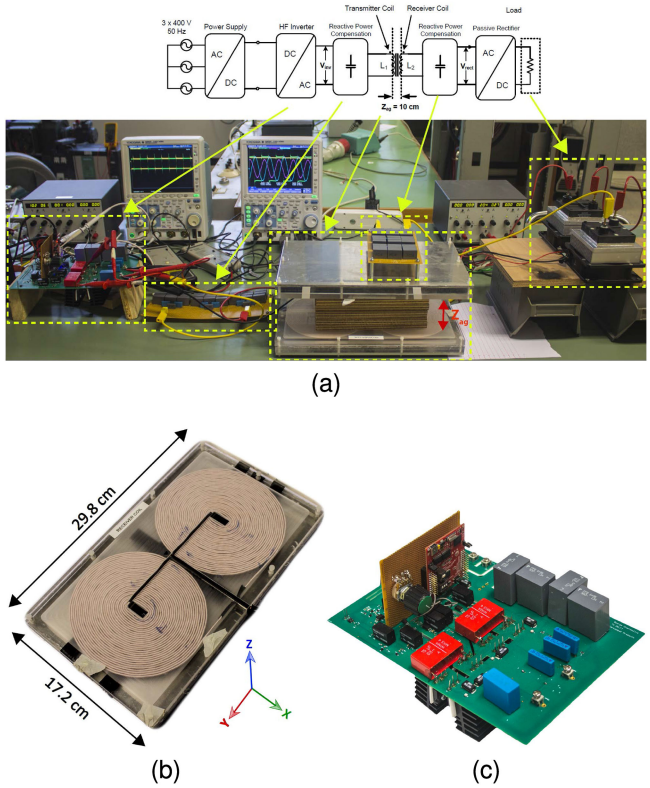

Fig. 5. (a) The overall experimental setup is shown along with the circuit schematic, (b) the dd coil setup is shown along with the dimensions. The receiver coil and the transmitter coil have similar design, (c) the SiC based H-bridge inverter is presented in this picture.

TABLE I
EXPERIMENTAL COMPONENT DETAILS

Semiconductors	SiC Cree: C2M008012D $R_{DS(on)}$ = 80 mΩ (25^o C)
Ferrite	Material type: P n_{fe} = 3
Litze	AWG 41 n_{str} = 525
Coils	DD-DD $N_T = N_R = 30$
Capacitor	Polypropylene film/foil tan δ = 0.2 [EPCOS]

setup is presented in Figure 5a. To simplify the experiments, a resistor is used instead of the battery. The resistive load is realized using low parasitic thick film power resistors (TAP1000 series) manufactured by OHMITE. Other details of the components used are presented in Table I.

A. Self-Inductance, Coupling, and Misalignment

The magnetic properties of the coils will be validated in this section. Table II shows the measured parameters at a nominal air gap of 10.2 cm and those obtained from the FE method along with the calculation error relative to the measured values. It can be observed that the self-inductances are calculated accurately

TABLE II
COMPARISON OF FE COMPUTED AND EXPERIMENTALLY OBTAINED CIRCUIT PARAMETERS

Variable	FE Model	Experiment	Error
L_1	211.2 µH	205.1 µH	+2.9 %
L_2	211.2 µH	198.7 µH	+6.2 %
M	31.4 µH	30.5 µH	+2.9 %
k	0.149	0.151	-1.5 %

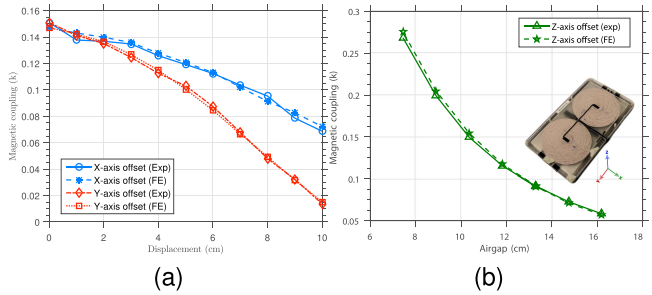

Fig. 6. Comparison of FE calculated magnetic coupling during misalignment with experiments. Variation of k with, (a) x-y misalignment with constant z-gap of 10 cm, (b) z-axis misalignment with perfect alignment in x-y axis.

by the used FE tool. The mutual inductance and magnetic coupling are also accurate with all absolute errors less than 10%. The negative error appears for the magnetic coupling, because in its calculation according to $k = \frac{M}{\sqrt{L_1 L_2}}$, the calculation errors in the self-inductance and the mutual inductance are combined. To validate the FE model over a wider operating range, the magnetic coupling is measured during misaligned conditions in all three axes. The results are compared to those obtained by the FE model and presented in Figure 6. It can be observed that the misalignment behavior of the coil system is calculated accurately by the FE model.

B. System Power Losses

Experiments are conducted to validate the loss models of the coils including the resonant capacitors and the power electronic devices. The total system loss is determined by post-processing the data extracted from waveforms at different operating points.

The experimentally obtained losses are compared with the model generated losses at different power levels. The collected data is presented with the aid of bar charts as shown in Figure 7. The data show good agreement between the experimental results and the model generated loss values with percentage error varying between 10% - 15%. The percentage error in loss estimation is 2-3 times compared to the percentage errors in parameter estimation (see Table II). This basically is due to error propagation as losses which depend on multiple parameters which in turn adds up to the error. Additionally, the model ignores the temperature dependence of copper resistivity. It uses the dc-resistance per unit length data provided by the litz wire manufacturer at 20 °C.

The distribution of the computed losses is also presented in the same plot. It is evident from the loss distribution bar charts that the capacitor dielectric is the dominant source of loss

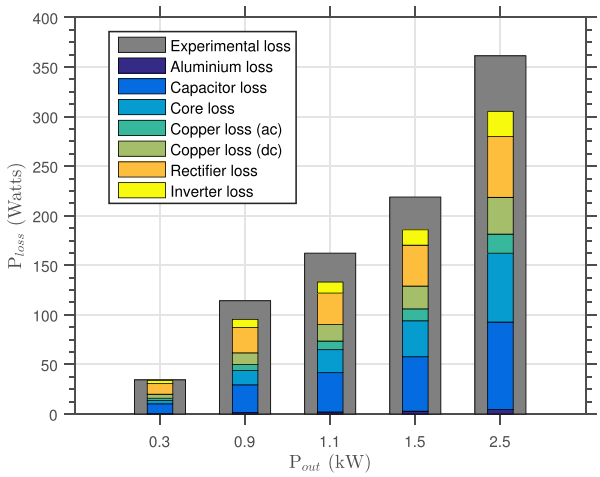

Fig. 7. Comparison of model computed losses with experimental loss data at different operating power at an airgap of 10 cm. The distribution of computed losses is also highlighted at different power levels. Computed losses are lower than experimentally determined losses with absolute average relative error of 15.2%.

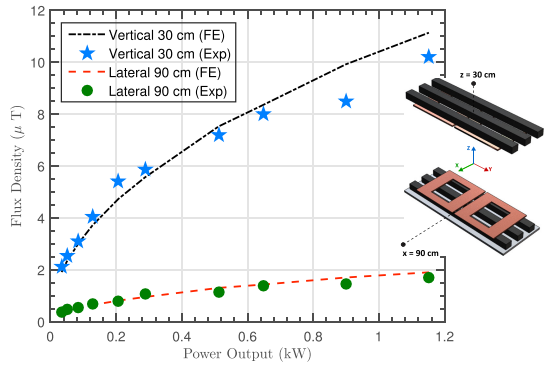

Fig. 8. Comparison of calculated and measured rms stray field of the IPT system at two different spots, namely 30 cm from the receiver coil center in the z-direction and 90 cm from the transmitter coil center in the x-direction. The average absolute value of the relative error with respect to the experimental values is 8.1%.

followed by ferrite core loss and copper losses. Shielding loss is almost negligible compared to other loss mechanisms which are in line with results reported in [12]. High capacitor dielectric losses can be attributed to the series-series compensation strategy which results in the capacitors carrying the full coupler driving currents.

C. Stray Field Measurement

Field measurements were taken with a field probe to validate the accuracy of the stray field calculation. The field probe used is EHP 50A manufactured by Narda. The comparison between rms stray field measurements and FE computed fields is presented in Figure 8 which shows reasonably good accuracy.

This concludes the experimental validation of the modeling strategy presented in Section II. The differences of the results obtained from the modeling approach are in good agreement with the experimentally obtained results (error of 3-5% in estimating the electro-magnetic parameters, 6-10% in stray field estimation, and 10-15% in predicting the overall system losses). Therefore, it can be concluded that couplers optimized using this simulator will perform as expected in practice. Next, this validated modeling strategy is utilized in a multi-objective optimization framework to fairly compare the different coupler concepts.

IV. Multi-Objective Optimization Framework and Results

A multi-objective optimization framework is developed in this section to compare the chosen coupler concepts. It utilizes the numerical modeling strategy developed in Section II and experimentally validated in Section III to evaluate the performance of the couplers. Initially, the system analysis flowchart is described followed by discussion on the optimization targets, variables, and constraints. Finally, the results of the optimization are presented and analyzed to compare among the coupler concepts.

A. System Analysis and Performance Parameters

Figure 9 shows the steps required to analyze a single IPT design in the optimization procedure. The system active mass (m_{sys}) includes the mass of the ferrite cores, litz wire winding, and the aluminum shielding. The gravimetric power density of the system is computed as : $\gamma = P_{\text{out}}/m_{\text{sys}}$. The area power density of the receiver coupler is calculated as: $\alpha = P_{\text{out}}/A_{\text{rec}}$ where A_{rec} is the receiver coupler area. The system losses are recomputed during misalignment to determine the misalignment efficiency (η_{mis}). Therefore, the misalignment efficiency difference of the design: $\delta\eta = \eta - \eta_{\text{mis}}$. This is used as a metric to judge the misalignment tolerance of a particular design. Lower the $\delta\eta$, more the misalignment tolerance of the design.

This concludes the modeling strategy of the coupler concepts along with the overall analysis of a single IPT design. Not all the steps are needed, depending on the objectives. The time required to evaluate a complete design varies between 3 mins - 6 mins.[1]

B. Optimization Targets and System Specifications

The coupler concepts are compared on the primary performance factors like efficiency, power densities, and misalignment performance. Based on that, the targets of the optimization are:

1) Maximize power transmission efficiency (η_{T})
2) Maximize gravimetric power density (γ)
3) Maximize receiver pad area power density (α)
4) Minimize misalignment efficiency difference $(\delta\eta)$

The objectives mentioned above are selected strategically to ensure that the optimization progresses towards designs with acceptable power densities and efficiency performance during both aligned and misaligned conditions. Table III shows the IPT system specifications. The optimization algorithm used for this problem is particle swarm optimization (PSO). PSO is an evolutionary gradient free algorithm inspired by the movement of birds or insects in swarm which is gradient free and potentially requires fewer function calls [31]. In this paper, an approach based on placing particles on the border of the search space using a combination of variable clipping and reflecting [31].

[1]Intel Xeon CPU E5-1620 v2 @ 3.70 GHz, 16 GB RAM.

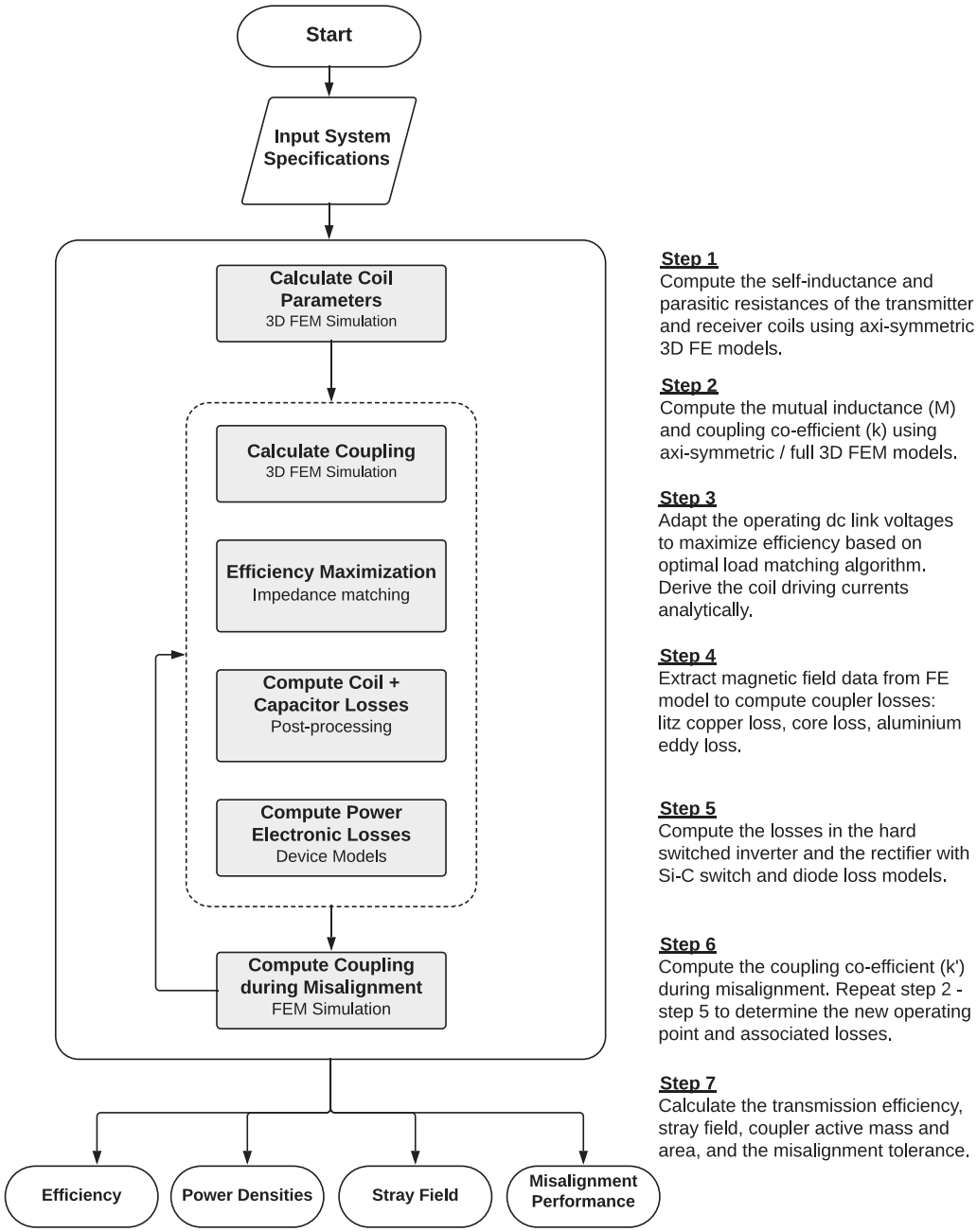

Fig. 9. System analysis flowchart for individual IPT designs during the optimization process.

TABLE III
IPT SYSTEM SPECFICATIONS

Symbol	Description	Value
δ	Operational air-gap	20 cm
P_{out}	Battery power requirement	7.2 kW
f	Operational frequency	85 kHz
U_{batt}	Nominal battery voltage	400 V
$U_{1,dc}$	Input dc link voltage	750 V
$U_{2,dc}$	Pick up dc link voltage	400-750 V
Δx	Lateral misalignment	$\pm$ 15 cm
Δy	Longitudinal misalignment	$\pm$ 20 cm

C. Optimization Variables and Constraints

The design variables of the optimization problem are all geometrical parameters of different coupler structures as shown in Figure 10. Ten geometrical parameters per coupler pad (transmitter and receiver) are optimized to ensure high design flexibility and exhaustive design space exploitation. The optimization variables and their range are presented in Table IV.

To ensure feasible designs, specific constraints are put on the optimization solution space as highlighted in Table V. A hard limit of 5A/mm^2 is placed on the litz wire current density to ensure thermal stability. To avoid bifurcation phenomena (multiple operating modes), limits on coil quality factors are placed

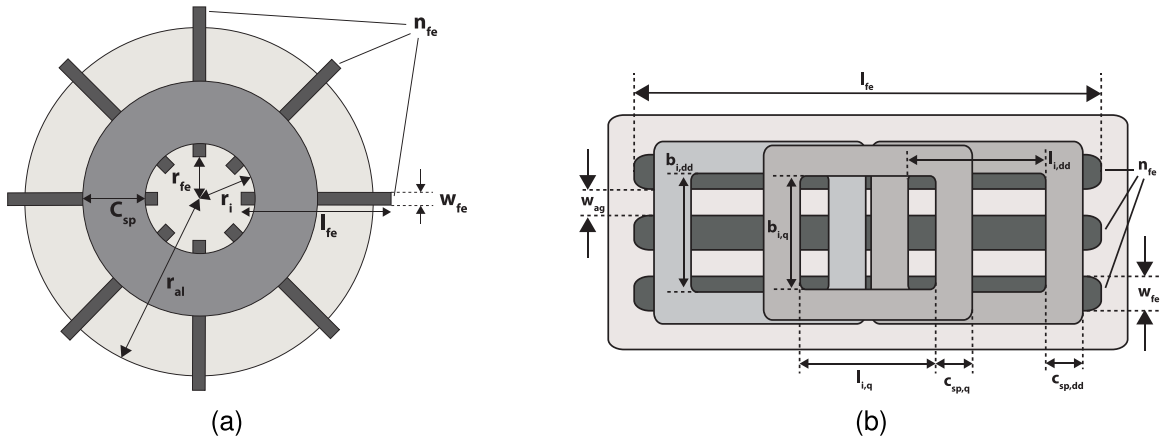

Fig. 10. Design variables for (a) circular coupler and (b) DDQ receiver pad topology. In both figures, the ferrite thickness (h_{fe}) is a variable which is not shown. The optimization variables of DD and rectangular couplers are similar to that of DDQ with the exception of the extra variables due to the Q coil. The coil spread parameter (C_{sp}) is defined as: $C_{\text{sp}} = N \times d$, where N is the number of turns and d is the external diameter of the litz wire which depends on the number of strands (n_{str}). The range of all the variables for different coupler geometries are presented in Table IV.

TABLE IV
OPTIMIZATION VARIABLES AND THEIR RANGE

Variable	Symbol	Unit	Range			
			DD-DD	DD-DDQ	Rect	Circ
Number of turns	N_{T}, N_{R}	-	15-60	15-60	20-65	20-65
Number of turns in Q coil	N_{Q}	-	-	15-60	-	-
Diameter of litz wire	d_{litz}	mm	2.4 - 4.8	2.4 - 4.8	2.4 - 4.8	2.4 - 4.8
Inner length	l_{i} , r_{i}	mm	10-35	10-35	10-75	10-75
Inner width	w_{i}	mm	10-35	10-35	10-75	-
Ferrite thickness	h_{fe}	mm	5-35	5-35	5-35	5-35
Ferrite width	w_{fe}	mm	15-45	15-45	15-45	15-45
Gap between ferrites[2]	w_{ag}	%	20-100	20-100	20-100	-
Length of ferrite [3]	l_{fe}	%	50-120	50-120	50-120	50-120
Number of ferrites	n_{fe}	-	1-7	1-7	1-7	2-12

TABLE V
OPTIMIZATION CONSTRAINTS

Symbol	Limit	Unit	Description
J	≤ 5	A/mm^2	Current density limit
k_{bi}	≥ 1.5	-	Bifurcation factor [32]
$B_{\text{fe,max}}$	≤ 35	mT	Maximum core flux density
$B_{\text{fe,avg}}$	≤ 20	mT	Average core flux density
$p_{\text{fe,density}}$	≤ 800	kW/m^3	Core loss density
η_{T}	≥ 93	%	Power transfer efficiency

by following bifurcation criterion proposed in [32]. The maximum flux density and the average flux density in the ferrite cores during misalignment operation is set to be 0.35 T and 0.2 T respectively (saturation flux density for 3C-90 core material is 0.45 T). In addition to that, a constraint is placed on the maximum core loss density at 800 kW/m^3 to ensure that the cores don't get overheated. To avoid wasting computational cycles on those designs, the global target in the PSO algorithm was selected from particles with at least 93 % efficiency. Coil designs which violate the above constraints are removed from the repository. Coil designs which violate the above constraints are removed from the repository.

This concludes the development of the MOO framework consisting of 20 design variables, 4 performance targets, and 6 constraints. The overall optimization is computationally expensive and requires solving 3000-4000 designs to arrive at stable Pareto fronts. The optimization results are discussed in the next section.

D. Results of Optimization

The optimization returns a 4D Pareto optimal front. To aid visualization and insight into the results, a detailed analysis is conducted in two steps. First, higher level results are analyzed using sub-fronts of two targets. At a second level, complete fronts are shown to aid explanation of underlying trends. Figure 11 and Figure 14 show the side views of the 4D Pareto optimal front which highlight the trade-offs between efficiency, misalignment difference, and power densities. To distinguish between the coupler shapes, only the sub-fronts are shown. These plots show the maximum achievable performance in one parameter only, disregarding the performance on other parameters. It means that

[2]100% means the outermost ferrite strips are at the edge of the coupler and 0% represents that all the ferrites are together forming a block in the center.

[3]Represented as a percentage of the total coil length.

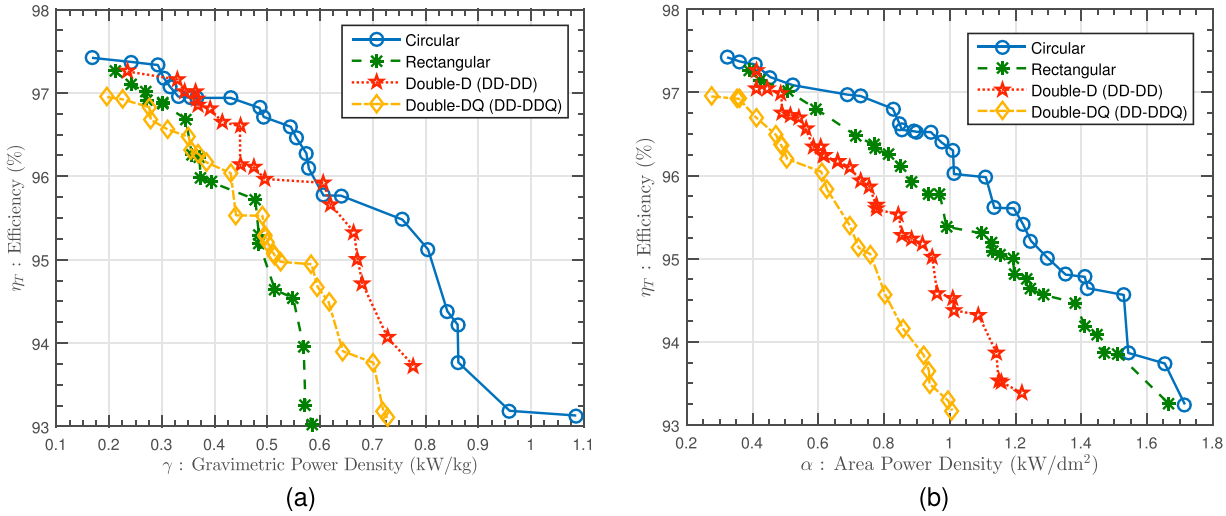

Fig. 11. Results of multi-objective optimization during perfect alignment operating conditions: (a) $\eta - \gamma$: pareto fronts of trade off between efficiency and gravimetric power density, (b) $\eta - \alpha$: pareto fronts of trade off between efficiency and receiver area power density.

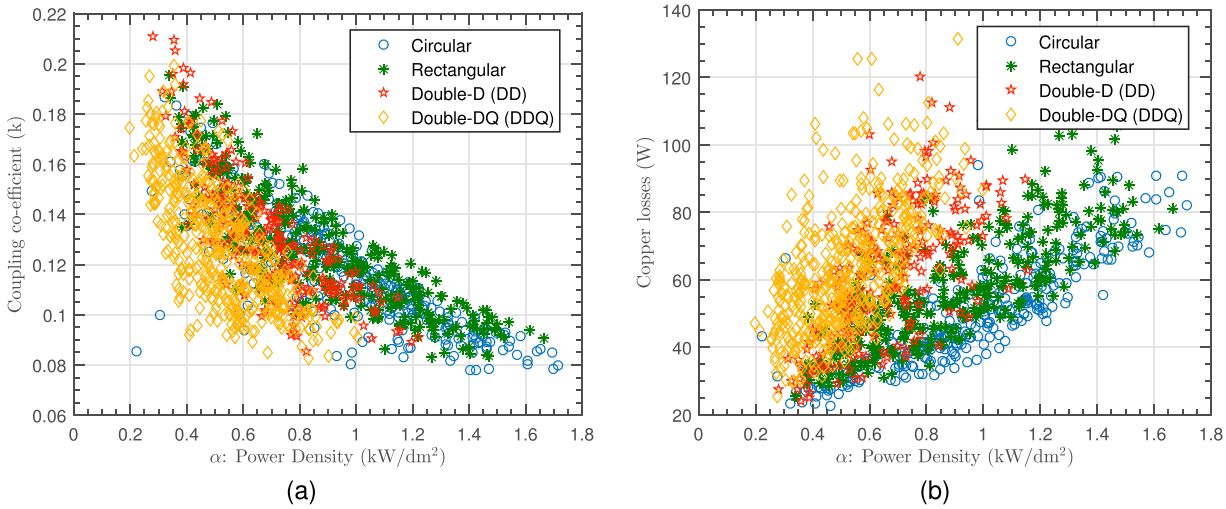

Fig. 12. Secondary performance factors during perfect alignment operating conditions of the optimal designs: (a) variation of coupling coefficient with receiver pad area power density, (b) total copper losses vs receiver pad area power density.

the designs located on, e.g., the $\eta - \gamma$ sub-front do not necessarily lie on the $\delta\eta - \alpha$. However, this representation can reveal strong or weak coupler shapes based on the goals, as well as provide insight into the limits of the performance goals individually. Based on the figures, some observations are drawn below:

Efficiency vs Gravimetric power density: Figure 11a show the Pareto fronts of efficiency during perfect alignment versus gravimetric power density of the couplers. The circular coupler is the best performer in this particular metric. This is due to higher coupling factors and lower ferrite core losses as shown in Figure 13b. It utilizes more ferrite material for the same gravimetric power density compared to other coils, as highlighted in Figure 13a. It leads to comparatively lower average flux density (B_{avg}) in the ferrite strips (see Figure 13c), thus leading to lower ferrite core losses. In addition to that, circular coils utilize less copper which leads to lower copper losses.

Rectangular couplers perform comparatively poorly compared to different coils in the η - γ front, due to the mismatch between the linear alignment of the ferrite strips and the fundamental flux pattern associated with a unipolar rectangular coil. Therefore, it has lower coupling co-efficient for the same gravimetric power density compared to other coil geometries. This leads to higher driving currents resulting in the increase of both copper losses and core losses.

The polarized couplers perform better than their rectangular counterpart in the $\eta - \gamma$ Pareto front since their fundamental flux pattern match with the linear arrangement of the ferrite strips in the polarized couplers. Therefore, they utilize ferrite material more efficiently unlike in the case of rectangular couplers. Within the polarized coupler family, the DD-DDQ coils perform comparatively worse than DD-DD coils in the $\eta - \gamma$ sub-fronts. This is expected since these performance parameters are computed during perfect alignment, and DD-DDQ couplers have added weight and area due to the Q-coil.

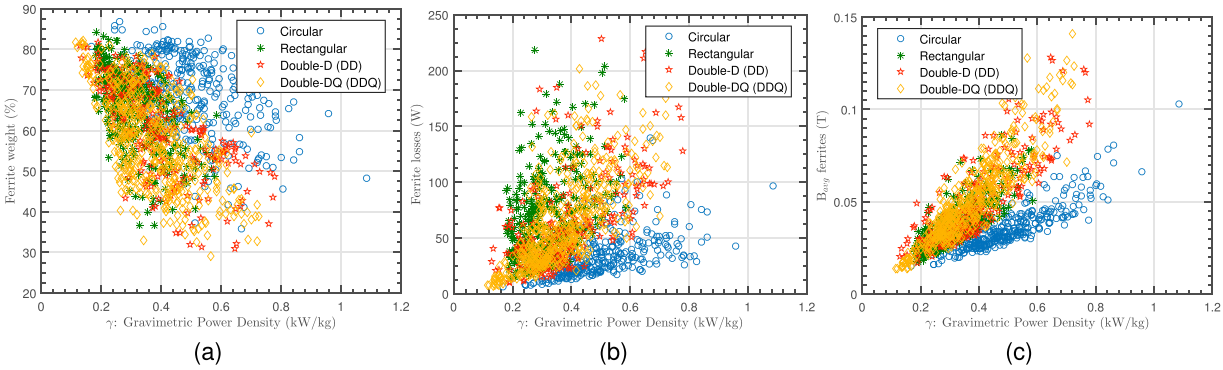

Fig. 13. Secondary performance factors during perfect alignment operating conditions of the optimal designs: (a) ferrite weight as a percentage of total coupler system weight, (b) total ferrite losses during perfect alignment, (c) average flux density in the ferrite strips.

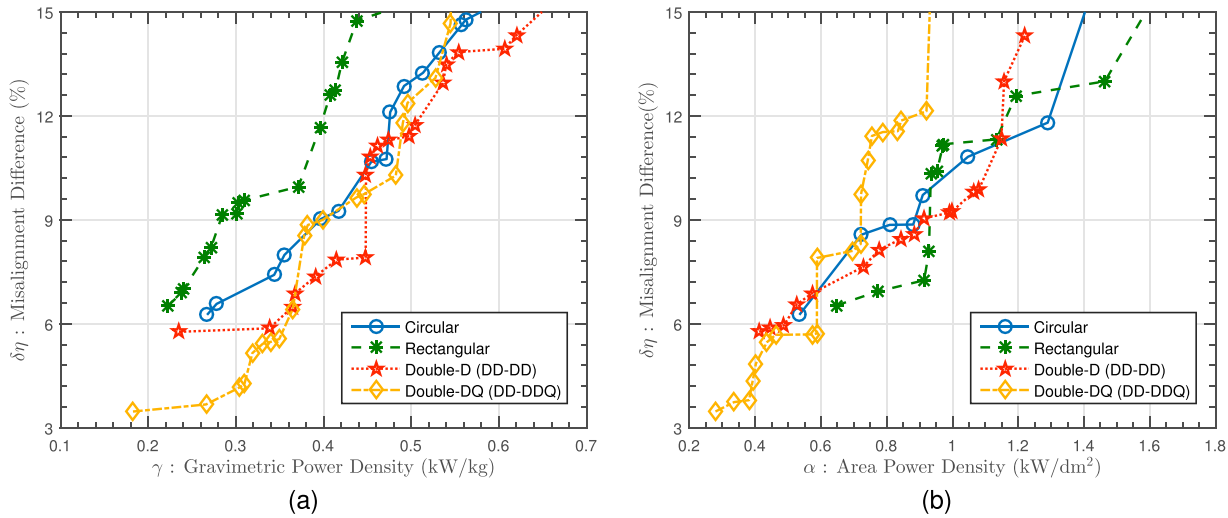

Fig. 14. The trade-offs between misalignment difference and power densities for the four coil concepts are shown in sub-front Pareto representation of (a) $\delta\eta - \gamma$, and (b) $\delta\eta - \alpha$.

Efficiency vs Receiver area power density: Figure 11b shows the Pareto fronts of efficiency versus receiver area power density. The non-polarized couplers perform much better than the polarized family in this performance metric. Higher coupling coefficients associated with non-polarized couplers for the same receiver pad area compared to their polarized counterpart (see Figure 12a) results in lower driving currents for the same power transfer. Therefore, copper losses in polarized couplers are lower than non-polarized couplers (see Figure 12b). It must be noted that Within the non-polarized family, circular couplers perform better than the rectangular couplers due to slightly lower copper losses.

It is evident from Figure 12a, that circular and rectangular couplers show higher attainable coupling k during aligned conditions for the same area power density (α) than bi-polar couplers like DD-DD and DD-DDQ which is in accordance with the results reported in [12], [16], [17]. However, several publications report that bi-polar pads like DD-DD have better coupling than circular couplers [5], [6], [13], [14]. It must be noted that the comparative analysis presented in those papers is based on conceptual arguments like fundamental flux height which depend on the specific parameters of each coupler design. In this paper, the couplers are optimized within certain design constraints which is not considered in the previous papers. The results obtained from this section show that using fundamental flux height as a metric to predict coupling of different coupler types is inaccurate.

However, it must be noted that the comparison trends derived from the presented optimization results are only applicable to circular couplers with radial ferrite distribution and rectangular, DD-DD, DD-DDQ couplers with longitudinal ferrite distribution. The general conclusions based on these trends might not be the same if only air-cored couplers are considered.

Misalignment tolerance vs Gravimetric power density: Figure 14a shows the $\delta\eta - \gamma$ front for all the coupler geometries. The polarized coupler family performs comparatively better than the non-polarized one in this metric. In the polarized family of couplers, the DD-DDQ coil performs marginally better than the DD-DD coil especially at lower gravimetric power densities ($<$0.4 kW/kg). However, at higher gravimetric power densities DD-DD coils perform similar to DD-DDQ. During misalignment condition, the Q-coil captures additional flux leading to higher values of

TABLE VI
SUMMARY OF COMPARISON OF IPT COUPLER SHAPES

Performance factors		Circ (T+R)	Rect (T+R)	DD (T+R)	DD (T) - DDQ (R)
Efficiency	vs Area	+	+/-	-	-
	vs Mass	+	-	+/-	-
Material effort[4]	Cu	+	+/-	-	-
	Fe	-	-	+	+
Stray field exposure[5]	Lateral	+	+/-	-	-
	Vertical	+/-	+	-	-
Misalignment tolerance	vs Area	+/-	+/-	+/-	-
	vs Mass	-	-	+/-	+

mutual inductance. Although DD-DDQ couplers have significantly higher mutual inductances during misalignment, their efficiency of power transfer doesn't show similar improvement due to additional losses incurred in the Q-coil and associated rectification circuit. Rectangular couplers perform poorly in the $\delta\eta - \gamma$ sub-front similar to their performance in the $\eta - \gamma$ sub-front. Circular couplers perform much better than rectangular couplers in this metric. However, DD-DD and DD-DDQ performs marginally better than circular couplers.

Misalignment tolerance vs Area power density: Figure 14b presents the $\delta\eta - \alpha$ front of the different coupler geometries. In the $\delta\eta - \alpha$ sub-front, the performance of all the considered coil topologies are comparable. The DD-DDQ coil doesn't perform similarly in the $\delta\eta - \alpha$ front compared to the $\delta\eta - \gamma$ front. It is penalized for higher coil area due to the Q-coil since the Q-coil tends to be larger than the individual DD coils due to high misalignment. Additionally, the DD-DDQ coil is only advantageous if misalignment occurs in the longitudinal direction (Y-axis) [5]. Therefore, the DD-DDQ coil performance is inferior to that of circular and rectangular coils since the design specifications (see Table III) also include significant misalignment in the lateral direction.

Stray magnetic field: The stray magnetic field generated by IPT couplers should comply with the guidelines set by ICNIRP [33]. It stipulates that the general public should not be exposed to RMS magnetic flux densities greater than 27μT (100μT for occupational exposure). In literature, authors have chosen different spatial points for spot measurements. Some examples are, 10 cm from the edge of a (1.5×1.5 m^2) vehicle [34], 110 cm from the airgap center point on the lateral direction [12], 30 cm from the receiver coil center in the vertical direction [20] etc. In this paper, two points are taken for spot flux density computation: (a) 30 cm from the receiver coil center in the vertical direction (z) and, (b) 90 cm from the transmitter coil center on the lateral direction (y). The stray flux densities of the Pareto designs for the different coils with coupling coefficient are shown in Figure 15. The non-polarized coils have significantly lower stray fields compared to the polarized family in the vertical direction. However, in EV applications

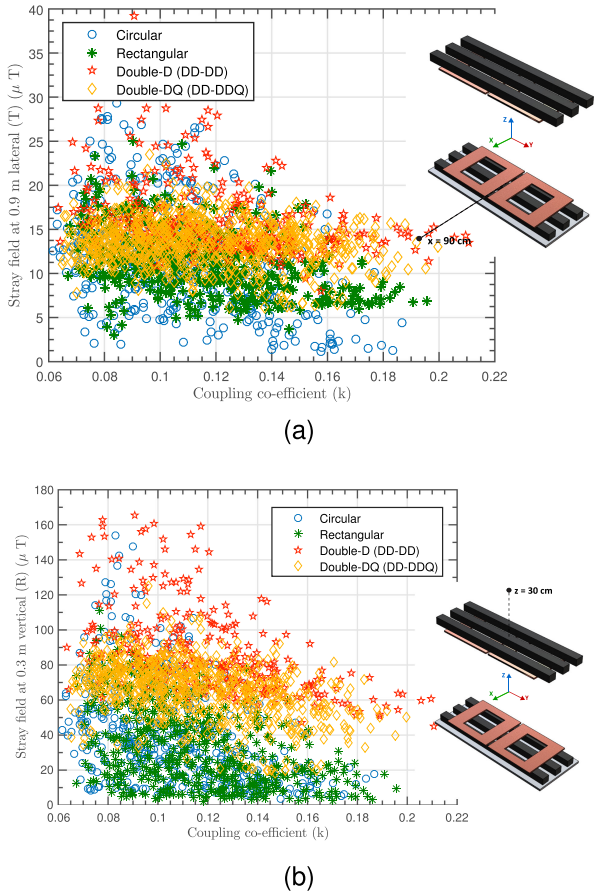

Fig. 15. Stray field behavior of different coil concepts during perfectly aligned operation with coupling coefficient. (a) Stray field computed at 0.9 m lateral (x-direction) from the transmitter coil center, and (b) Stray field computed at 0.3 m vertical (z-direction) from the receiver coil center. The aluminum shielding on the receiver pad is not shown but considered.

there will be an aluminum vehicle body which will reduce this stray field value. In the lateral direction, non-polarized couplers have slightly lower stray fields compared to polarized couplers.

Table VI provides a summary of the detailed quantitative comparison and highlights the relative advantages and disadvantages of each coupler types in terms of efficiency, power densities, material effort, stray field and misalignment performance. It must be noted that the performance factors analysed

[4]Positive grades like '+' in this metric means lower requirement of material for the same performance.

[5]Positive grades like '+' in this metric means lower stray field.

in IPT systems are mutually conflicting in nature. Therefore, the relative grades assigned to individual coupler shapes represent the absolute maximum performance in only that category. This concludes a detailed comparative analysis of the primary and secondary performance parameters of the considered coil topologies.

V. Conclusion

This paper presents a holistic comparison of four coupler concepts: circular, rectangular, DD-DD, and DD-DDQ. The main advantages and disadvantages of the four IPT coupler concepts are discussed with multi-objective Pareto analysis. Detailed experiments are conducted on a laboratory prototype to validate the models. Thus, the analysis is accurate. Some important results obtained are:

1) Circular couplers have the best efficiencies and coupling k for the same gravimetric power density (γ) among all concepts followed by DD-DD and DD-DDQ during perfectly aligned conditions. Rectangular couplers perform poorly in this metric and thus lead to heavier designs for the same efficiency.
2) Circular couplers use the most ferrite material and the least copper material among all the coupler topologies for the same performance.
3) The circular and rectangular couplers outperform the polarized couplers for the same receiver area power density (α), with higher power transmission efficiency by 1%-4%. This is caused by higher average core flux densities and lower absolute coupling k in the polarized couplers.
4) When misaligned, the performance gap between the two coupler families, reduces with DD-DDQ outperforming other coil topologies with lower misalignment difference for the same γ. Its multi-coil geometry makes it tolerant to misalignment with complementary flux capture by the Q coil.
5) The circular and rectangular couplers have lower stray flux densities compared to polarized DD-DD and DD-DDQ couplers in both lateral and vertical direction.

In conclusion, the presented multi-objective IPT optimization process provides a platform for systematic comparison of all the popular coupler concepts which allows Pareto tradeoffs to be taken into account during the initial design phase. In IPT applications without misalignment, circular coupler provides the best performance. Optimized circular couplers are more efficient, lighter, and smaller compared to all other topologies. Besides, they have lower leakage flux in both vertical and lateral direction. However, in IPT applications requiring misalignment operation, DD-DDQ provides better performance compared to other topologies.

Appendix

Proof of Optimal Load Impedance Matching Condition

The optimal load impedance matching condition (9) for an IPT system with asymmetric coil designs is derived here. At this condition, the efficiency of power transfer from the transmitter coupler to the receiver coupler is maximum. The equivalent circuit of a double coil IPT system is shown in Figure 16.

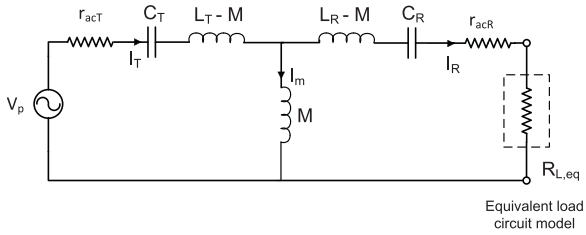

Fig. 16. Equivalent circuit of the magnetic link of the IPT system.

Based on the analysis in [35], the load circuit of the pick-up or receiver side is modelled as an equivalent load resistance:

$$R_{\mathrm{L,eq}} = \frac{8}{\pi^2 \eta_{\mathrm{rec}}} \frac{U_{2,\mathrm{dc}}^2}{P_{\mathrm{out}}} \tag{12}$$

During resonance operation, the transmitter and the receiver currents $(I_{\mathrm{T,R}})$ have only active components. Therefore, the efficiency of power transfer can be expressed as the following:

$$\eta = \frac{I_{\mathrm{R}}^2 R_{\mathrm{L,eq}}}{I_{\mathrm{R}}^2 R_{\mathrm{L,eq}} + I_{\mathrm{R}}^2 r_{\mathrm{acR}} + I_{\mathrm{T}}^2 r_{\mathrm{acT}}} \tag{13}$$

where the transmitter and the receiver currents are expressed as the following:

$$I_{\mathrm{T}} = \frac{V_{\mathrm{p}}(R_{\mathrm{L,eq}} + r_{\mathrm{acR}})}{\omega^2 M^2 + R_{\mathrm{L,eq}} r_{\mathrm{acT}} + r_{\mathrm{acR}} r_{\mathrm{acT}}} \tag{14}$$

$$I_{\mathrm{R}} = \frac{\omega M V_{\mathrm{p}}}{\omega^2 M^2 + R_{\mathrm{L,eq}} r_{\mathrm{acT}} + r_{\mathrm{acR}} r_{\mathrm{acT}}} \tag{15}$$

Combining equations (13), (14), (15), the efficiency can be expressed as:

$$\eta = \frac{\omega^2 M^2 R_{\mathrm{L,eq}}}{(R_{\mathrm{L,eq}} + r_{\mathrm{acR}})(\omega^2 M^2 - R_{\mathrm{L,eq}} r_{\mathrm{acT}} - r_{\mathrm{acR}} r_{\mathrm{acT}})} \tag{16}$$

The design condition of maximum efficiency at any operating point is achieved when:

$$\frac{\partial \eta}{\partial R_{\mathrm{L,eq}}} = \frac{\omega^2 M^2 (\omega^2 M^2 r_{\mathrm{acR}} - r_{\mathrm{acT}} R_{\mathrm{L,eq}}^2 + r_{\mathrm{acT}} r_{\mathrm{acR}}^2)}{(R_{\mathrm{L,eq}} + r_{\mathrm{acR}})^2 (\omega^2 M^2 - R_{\mathrm{L,eq}} r_{\mathrm{acT}} - r_{\mathrm{acR}} r_{\mathrm{acT}})^2} = 0 \tag{17}$$

Solving the above equation, the load matching factor of IPT systems with asymmetric coils is obtained as following:

$$R_{\mathrm{L,eq}} = \sqrt{\omega^2 M^2 \frac{r_{\mathrm{acR}}}{r_{\mathrm{acT}}} + r_{\mathrm{acR}}^2} \tag{18}$$

which can be simplified as:

$$R_{\mathrm{L,eq}} \approx \omega M \sqrt{\frac{r_{\mathrm{acR}}}{r_{\mathrm{acT}}}} \tag{19}$$

References

[1] K. Van Schuylenbergh and R. Puers, *Inductive Powering: Basic Theory and Application to Biomedical Systems*. New York, NY, USA: Springer, 2009.

[2] D. Patil, M. K. McDonough, J. M. Miller, B. Fahimi, and P. T. Balsara, "Wireless power transfer for vehicular applications: Overview and challenges," *IEEE Trans. Transp. Electrific.*, vol. 4, no. 1, pp. 3–37, Mar. 2018.

[3] G. A. Covic and J. T. Boys, "Modern trends in inductive power transfer for transportation applications," *IEEE J. Emerg. Sel. Topics Power Electron.*, vol. 1, no. 1, pp. 28–41, Mar. 2013.
[4] S. Jeong, Y. J. Jang, and D. Kum, "Economic analysis of the dynamic charging electric vehicle," *IEEE Trans. Power Electron.*, vol. 30, no. 11, pp. 6368–6377, Nov. 2015.
[5] M. Budhia, J. T. Boys, G. A. Covic, and C.-Y. Huang, "Development of a single-sided flux magnetic coupler for electric vehicle IPT charging systems," *IEEE Trans. Ind. Electron.*, vol. 60, no. 1, pp. 318–328, Jan. 2013.
[6] G. A. Covic, M. L. Kissin, D. Kacprzak, N. Clausen, and H. Hao, "A bipolar primary pad topology for EV stationary charging and highway power by inductive coupling," in *Proc. IEEE Energy Convers. Congr. Expo.*, 2011, pp. 1832–1838.
[7] S. Raabe, G. Elliott, G. Covic, and J. Boys, "A quadrature pickup for inductive power transfer systems," in *Proc. IEEE Conf. Ind. Electron. Appl.*, 2007, pp. 68–73.
[8] S. Y. Jeong, S. Y. Choi, M. Sonapreetha, and C. T. Rim, "DQ-quadrature power supply coil sets with large tolerances for wireless stationary EV chargers," in *Proc. IEEE PELS Workshop Emerg. Technol., Wireless Power*, 2015, pp. 1–6.
[9] Y. Nagatsuka, N. Ehara, Y. Kaneko, S. Abe, and T. Yasuda, "Compact contactless power transfer system for electric vehicles," in *Proc. Int. Power Electron. Conf.*, 2010, pp. 807–813.
[10] M. Budhia, G. A. Covic, and J. T. Boys, "Design and optimization of circular magnetic structures for lumped inductive power transfer systems," *IEEE Trans. Power Electron.*, vol. 26, no. 11, pp. 3096–3108, Nov. 2011.
[11] G. Buja, M. Bertoluzzo, and K. N. Mude, "Design and experimentation of WPT charger for electric city car," *IEEE Trans. Ind. Electron.*, vol. 62, no. 12, pp. 7436–7447, Dec. 2015.
[12] R. Bosshard and J. W. Kolar, "Multi-objective optimization of 50 kW/85 KHz IPT system for public transport," *IEEE J. Emerg. Sel. Topics Power Electron.*, vol. 4, no. 4, pp. 1370–1382, Dec. 2016.
[13] G. R. Nagendra, G. A. Covic, and J. T. Boys, "Determining the physical size of inductive couplers for IPT EV systems," *IEEE J. Emerg. Sel. Topics Power Electron.*, vol. 2, no. 3, pp. 571–583, Sep. 2014.
[14] A. Zaheer, D. Kacprzak, and G. A. Covic, "A bipolar receiver pad in a lumped IPT system for electric vehicle charging applications," in *Proc. IEEE Energy Convers. Congr. Expo.*, 2012, pp. 283–290.
[15] S. Bandyopadhyay, V. Prasanth, L. R. Elizondo, and P. Bauer, "Design considerations for a misalignment tolerant wireless inductive power system for electric vehicle (EV) charging," in *Proc. IEEE Energy Convers. Congr. Expo.*, 2017, pp. 1–10.
[16] K. Knaisch and P. Gratzfeld, "Comparison of magnetic couplers for inductive electric vehicle charging using accurate numerical simulation and statistical methods," in *Proc. Elect. Drives Prod. Conf.*, 2015, pp. 1–10.
[17] K. Knaisch, M. Springmann, and P. Gratzfeld, "Comparison of coil topologies for inductive power transfer under the influence of ferrite and aluminum," in *Proc. Ecol. Veh. Renewable Energies*, 2016, pp. 1–9.
[18] V. Prasanth, S. Bandyopadhyay, P. Bauer, and J. A. Ferreira, "Analysis and comparison of multi-coil inductive power transfer systems," in *Proc. IEEE Power Electron. Motion Control Conf.*, 2016, pp. 993–999.
[19] R. Bosshard, U. Iruretagoyena, and J. W. Kolar, "Comprehensive evaluation of rectangular and double-D coil geometry for 50 kW/85 KHz IPT system," *IEEE J. Emerg. Sel. Topics Power Electron.*, vol. 4, no. 4, pp. 1406–1415, Dec. 2016.
[20] R. Bosshard, J. W. Kolar, J. Mühlethaler, I. Stevanović, B. Wunsch, and F. Canales, "Modeling and η-α-Pareto optimization of inductive power transfer coils for electric vehicles," *IEEE J. Emerg. Sel. Topics Power Electron.*, vol. 3, no. 1, pp. 50–64, Mar. 2015.
[21] S. Bandyopadhyay, V. Prasanth, P. Bauer, and J. Ferreira, "Multi-objective optimisation of a 1-kW wireless IPT systems for charging of electric vehicles," in *Proc. IEEE Transp. Electrific. Conf. Expo*, 2016, pp. 1–7.
[22] T. Nakata, N. Takahashi, K. Fujiwara, and A. Ahagon, "Periodic boundary condition for 3-D magnetic field analysis and its applications to electrical machines," *IEEE Trans. Magn.*, vol. 24, no. 6, pp. 2694–2696, Nov. 1988.
[23] J. Mühlethaler, "Modeling and multi-objective optimization of inductive power components," Ph.D. dissertation, Dept. Power Electron. Syst. Lab., ETH Zurich, ETH Zurich, Zürich, Switzerland, 2012.
[24] C. P. Steinmetz, "On the law of hysteresis," *Proc. IEEE*, vol. 72, no. 2, pp. 197–221, Feb. 1984.
[25] COMSOL Multiphysics, "v. 5.2," COMSOL AB, Stockholm, Sweden, 2015.
[26] M. Brubaker, H. Kirbie, T. Hosking, and T. Von Kampen, "System level considerations for integration of resonant capacitors in high power wireless charging," in *Proc. Conf. Elect. Roads Veh.*, 2012.
[27] T. Diekhans, F. Stewing, G. Engelmann, H. van Hoek, and R. W. De Doncker, "A systematic comparison of hard-and soft-switching topologies for inductive power transfer systems," in *Proc. Elect. Drives Prod. Conf.*, 2014, pp. 1–8.
[28] K. Peng and E. Santi, "Performance projection and scalable loss model of SiC MOSFETs and SiC Schottky diodes," in *Proc. Elect. Ship Technol. Symp.*, 2015, pp. 281–286.
[29] T. Diekhans and R. W. De Doncker, "A dual-side controlled inductive power transfer system optimized for large coupling factor variations and partial load," *IEEE Trans. Power Electron.*, vol. 30, no. 11, pp. 6320–6328, Nov. 2015.
[30] D. Kobayashi, T. Imura, and Y. Hori, "Real-time coupling coefficient estimation and maximum efficiency control on dynamic wireless power transfer for electric vehicles," in *Proc. IEEE PELS Workshop Emerg. Technol., Wireless Power*, 2015 pp. 1–6.
[31] Y. Del Valle, G. K. Venayagamoorthy, S. Mohagheghi, J.-C. Hernandez, and R. G. Harley, "Particle swarm optimization: Basic concepts, variants, and applications in power systems," *IEEE Trans. Evol. Comput.*, vol. 12, no. 2, pp. 171–195, Apr. 2008.
[32] C.-S. Wang, G. A. Covic, and O. H. Stielau, "Power transfer capability and bifurcation phenomena of loosely coupled inductive power transfer systems," *IEEE Trans. Ind. Electron.*, vol. 51, no. 1, pp. 148–157, Feb. 2004.
[33] J. Lin *et al.*, "ICNIRP guidelines for limiting exposure to time-varying electric and magnetic fields (1 Hz to 100 KHz)," *Health Phys.*, vol. 99, pp. 818–836, 2010.
[34] F. Y. Lin, G. A. Covic, and J. T. Boys, "Evaluation of magnetic pad sizes and topologies for electric vehicle charging," *IEEE Trans. Power Electron.*, vol. 30, no. 11, pp. 6391–6407, Nov. 2015.
[35] R. L. Steigerwald, "A comparison of half-bridge resonant converter topologies," *IEEE Trans. Power Electron.*, vol. 3, no. 2, pp. 174–182, Apr. 1988.

Soumya Bandyopadhyay received the B.Tech. degree (first-class Hons.) in electrical and electronics engineering from Jadavpur University, Kolkata, India, in 2011, and the M.Sc. degree in electrical engineering from the Delft University of Technology, Delft, The Netherlands, in 2015. Since 2016, he has been working toward the Ph.D. degree in the field of key power electronics in low-voltage dc distribution systems. His research interests include multiport DC–DC converter design for renewable sources and storages, smart charging of electric vehicles, and wireless power transfer.

Prasanth Venugopal (S'13–M'17) received the B.Tech. degree in electrical and electronics engineering from Amrita Vishwa Vidyapeetham University (silver medal), Coimbatore, India, in 2010, and the M.Sc. degree *(cum laude)* in electrical engineering and the Ph.D. degree in magnetic energy transfer in roads from the Delft University of Technology, Delft, The Netherlands, in 2012 and 2016, respectively.

From September 2016 to December 2018, he was with the Qualcomm Halo, Munich, Germany, as a Senior Electrical Engineer in the field of power electronic systems and applications. He is currently with the TDK Europe Gmbh, Munich, Germany, as a Technical Specialist for xEV applications. He has filed six patent applications, which are at various stages of acceptance. He is interested in application of electromagnetic field theory to the areas of power electronics and its control so as to produce innovative solutions.

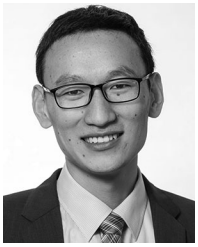

Jianning Dong received the B.S. and Ph.D. degrees in electrical engineering from Southeast University, Nanjing, China, in 2010 and 2015, respectively. He was a Postdoctoral Researcher with the McMaster Automotive Resource Centre, McMaster University, Hamilton, ON, Canada. Since 2016, he has been an Assistant Professor with the Delft University of Technology, Delft, The Netherlands. His research interests are wireless power transfer and electromechanical systems.

Pavol Bauer (SM'07) received master's degree in electrical engineering from the Technical University of Kosice, Kosice, Slovakia, in 1985, and the Ph.D. degree from the Delft University of Technology, Delft, The Netherlands, in 1995.

He is currently a Full Professor with the Department of Electrical Sustainable Energy, Delft University of Technology, and the Head of DC Systems, Energy Conversion and Storage Group. From 2002 to 2003, he was working partially with KEMA (DNV GL, Arnhem, The Netherlands) on different projects related to power electronics applications in power systems. He has authored or coauthored more than 95 journal and more than 300 conference papers in his field (with H factor Google scholar 35, Web of science 23). He is an author or co-author of eight books, holds four international patents, and organized several tutorials at the international conferences. He has worked on many projects for industry concerning wind and wave energy, power electronic applications for power systems such as Smarttrafo, HVdc systems, projects for smart cities such as photovoltaic (PV) charging of electric vehicles, PV and storage integration, contactless charging. He has participated in several Leonardo da Vinci and H2020 EU projects as a Project Partner (ELINA, INETELE, E-Pragmatic) and a Coordinator (PEMCWebLab.com-Edipe, SustEner, Eranet DCMICRO).

Dr. Bauer is the Former Chairman of Benelux IEEE Joint Industry Applications Society, Power Electronics and Power Engineering Society Chapter, the Chairman of the Power Electronics and Motion Control Council, a member of the Executive Committee of European Power Electronics Association, and also a member of the International Steering Committee at numerous conferences. He was a recipient of the Title Professor from the President of Czech Republic at the Brno University of Technology, Brno, Czech Republic, in 2008, and the Delft University of Technology, in 2016.